ACS APPLIED MATERIALS & INTERFACES

www.acsami.org

Research Article

Composition-Dependent Li-Ion Transport in Mixed-Metal ZIF-62 Glasses Revealed by Machine-Learning Molecular Dynamics

Ram Sewak* and Anirban Mondal*

Cite This: https://doi.org/10.1021/acsami.6c03442

Read Online

ACCESS | Metrics & More | Article Recommendations | Supporting Information

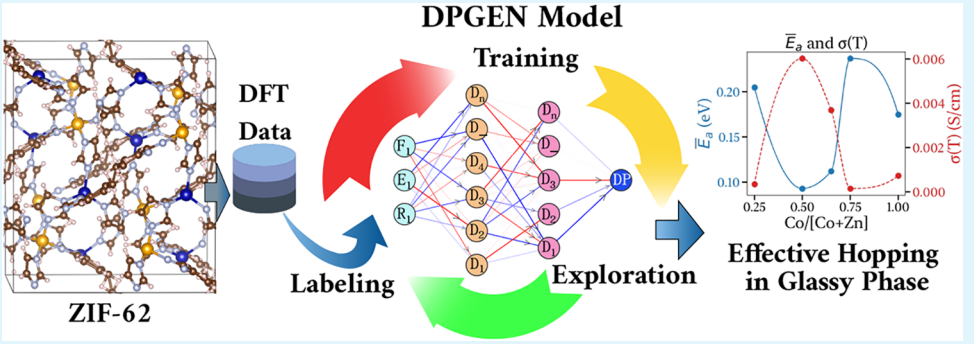

ABSTRACT: Understanding ion transport in metal−organic frameworks requires resolving the interplay between framework dynamics, local disorder, and thermally activated hopping on extended time and length scales. Here, we develop a robust deep neural network (DNN) interatomic potential, trained and validated against density functional theory data using the DP-GEN framework, to investigate Li-ion transport in pure and mixed-metal ZIF-62 across a wide range of Co/(Co + Zn) ratios. Large-scale deep potential molecular dynamics simulations at 450 K reveal that Li-ion motion is governed by localized vibrational dynamics within metastable cages, punctuated by activated hopping events through the interconnected pore network. Van Hove correlation analysis reveals that intermediate metal substitution [Co/(Co + Zn) ≈ 0.25−0.50] optimizes the spatial extent of Li displacements while maintaining a stable local coordination environment. Jump-resolved analysis further demonstrates that the 0.50−ZIF−62 composition exhibits the lowest effective activation energy (~0.093 eV) and the highest ionic conductivity (~6.0×10^{-3} S cm^{-1}), arising from a dynamically evolving, composition-dependent energy landscape. Correlated-motion analysis indicates that long-range diffusion proceeds predominantly via independent hopping rather than sustained collective migration. Together, these results establish a unified and dynamic picture of Li-ion transport in mixed-metal MOF electrolytes, demonstrating the predictive capability of machine-learning interatomic potentials for the rational design of high-conductivity solid-state ion conductors.

KEYWORDS: *Metal−organic frameworks (MOFs), MOF glasses, Deep neural network potentials, Machine-learning molecular dynamics, Lithium-ion transport, Ionic conductivity*

1. INTRODUCTION

Lithium-ion batteries (LIBs) have become the cornerstone of modern energy storage technologies, powering portable electronics, electric vehicles, and even aircraft due to their high energy density and long cycle life.[1−5] Despite these advantages, conventional LIBs still face persistent challenges. The limited thermal stability of separators and the growth of lithium dendrites, especially in lithium−metal batteries (LMBs), pose serious safety risks and reduce operational reliability.[6,7] Moreover, meeting the increasing demand for high power density, fast charge−discharge rates, and extended cycle life requires continuous optimization of electrolyte materials and electrode−electrolyte interfaces.[8−11] Since these electrochemical characteristics are strongly dictated by structural features such as porosity, surface area, and ionic conductivity, designing materials with tunable and efficient ion transport pathways remains a central objective in next-generation battery research.[12]

Among the emerging materials, metal−organic frameworks (MOFs) offer a unique opportunity to address these limitations owing to their exceptional structural and chemical tunability.[13] MOFs are crystalline porous solids consisting of metal-containing nodes—secondary building units (SBUs)—connected by multidentate organic ligands via coordination bonds. Their modular design enables the deliberate tuning of

Received: February 16, 2026
Revised: April 9, 2026
Accepted: April 16, 2026

framework topology and functionality, allowing nearly unlimited combinations of pore architectures and surface chemistries. Beyond their well-defined crystalline architectures, MOFs can undergo order−disorder and solid−liquid−glass transitions that, while reducing intrinsic porosity, generate dense and moldable glasses with distinctive mechanical and electrochemical properties.[14,15] This reticular design approach, coupled with coordination versatility, offers features rarely accessible in conventional inorganic or polymeric electrolytes.

Crystalline MOFs offer exceptionally high surface areas and chemically tunable pores,[16,17] yet their intrinsic anisotropy and grain boundaries often impede uniform ion transport. In contrast, glassy MOFs feature isotropic, grain-boundary-free networks that enable smooth and dendrite-free lithium plating and stripping.[18,19] These amorphous derivatives preserve the structural versatility of MOFs while gaining the processability of glasses, allowing precise control over pore architecture, metal nodes, and linker functionality to regulate lithium mobility and interfacial chemistry.[12,20−23] Consequently, MOFs have been successfully employed as anode coatings forming semisolid interphases with high ion diffusivity, as electrolyte additives that immobilize bulky anions to improve cation transference, and as components of hybrid polymer−MOF systems that guide lithium nucleation and suppress dendrite growth.[24,25]

Despite the availability of over 100,000 reported MOF structures,[26] only a small subset can be melt-quenched into glass. Among these, zeolitic imidazolate frameworks (ZIFs)—composed of Zn^{2+}/Co^{2+} nodes coordinated by imidazolate linkers—are particularly notable because they melt prior to decomposition.[27−29] A limited number of ZIFs, including ZIF-4, ZIF-62, and related analogues (e.g., TIF-4, ZIF-UC-1−5, ZIF-zni, $Zn(im)_2$, and MUV-24), exhibit glass-forming ability upon melt quenching.[30−34] Among them, ZIF-62 has emerged as the prototypical MOF glass due to its mixed imidazole/benzimidazole linker chemistry and exceptional glass-forming ability.[35] The bulky benzimidazole units enlarge ion-transport channels and enhance Li^+ mobility, as evidenced by the high lithium-storage capacity of Co−ZIF-62 anodes (306 mAh g^{-1} after 1000 cycles at 2 A g^{-1}) and the dendrite-free interfacial transport observed in Zn-based ZIF-62 coatings.[36,37]

Tuning ZIF composition provides a robust handle to control melting behavior, porosity, and local coordination environments. Adjusting the imidazolate/benzimidazolate ratio[38] or introducing mixed-metal nodes such as Co/Zn[39] can modulate the glass-transition-to-melting temperature ratio (T_g/T_m) and influence both bond strength and network flexibility. However, how such compositional tuning impacts Li-ion transport at the atomic level remains poorly understood, primarily because the disordered nature of glassy ZIFs challenges conventional simulation methods. While *ab initio* molecular dynamics (AIMD) provides accurate insights into local structure and energetics, it is computationally prohibitive for the extended time scales required to capture ion migration. Classical force-field simulations, on the other hand, lack the fidelity to describe metal−ligand coordination and framework flexibility. We develop machine-learning force fields (MLFFs) to overcome these limitations based on deep neural networks trained on density-functional-theory (DFT) reference data. This approach enables us to simulate Li-ion diffusion in pure and mixed-metal ZIF-62 glasses with near-DFT accuracy and substantially greater efficiency.

Our simulations at 450 K reveal that Li^+ motion involves localized vibrations around metastable sites, accompanied by intermittent long-range hopping. The mixed-metal (0.50−ZIF-62) composition exhibits the largest atomic displacements, lowest activation energy (~0.093 eV), and highest ionic conductivity (~6.0×10^{-3} S/cm), underscoring the synergistic role of metal-node substitution in facilitating ion transport. Correlated motion analysis further indicates that Li diffusion proceeds via independent hopping along the intrinsic pore network of the glassy framework. In summary, this work introduces a transferable machine-learning framework for modeling complex ion-transport processes in MOF-derived solid-state electrolytes. By combining the compositional tunability of mixed-metal ZIF-62 glasses with the precision of neural-network potentials, we uncover the microscopic origins of enhanced lithium mobility—providing molecular-level design principles for next-generation solid electrolytes.

2. METHODS

2.1. Preparation of ZIF-62 Systems and AIMD Data Set Generation

Building on the insights gained from our introduction, the next stage of this study focuses on constructing realistic atomistic models and generating high-fidelity reference data to develop a machine-learning potential capable of capturing Li-ion dynamics in glassy ZIF-62 systems. Given that the composition and local coordination of metal nodes significantly influence structural flexibility and ion transport, both pristine and mixed-metal ZIF-62 models were considered to systematically probe the role of metal substitution on the potential-energy landscape and Li^+ mobility.

The initial atomic configuration of crystalline ZIF-62 was obtained from the Cambridge Structural Database (CSD; CCDC No. 671070). The crystal adopts an orthorhombic structure (space group *Pbca*) in which tetrahedrally coordinated metal ions are linked by three imidazolate and one benzimidazolate ligands. To explore the compositional dependence of Li-ion behavior, two unit-cell models of the ZIF-62 framework were constructed: (i) a pristine system containing only Co nodes (1.00−ZIF-62), and (ii) a mixed-metal system in which 37.5% of the Co nodes were substituted with Zn (0.625−ZIF-62). Each model was subsequently doped with six Li^+ ions and six $TFSI^-$ ions, randomly placed within the accessible pore regions of the ZIF-62 framework. The resulting structures were then fully relaxed to obtain energetically stable configurations for subsequent simulations. The mixed-metal node composition was chosen based on previous studies of the Co/Zn−ZIF-62 series,[39] which systematically showed that metal substitution strongly affects thermodynamic, kinetic, and mechanical properties. In particular, compositions of Co/(Co + Zn) near 0.6 exhibit the lowest glass transition temperature (T_g), providing experimental motivation for the selected model.

To train a robust and transferable machine-learning interatomic potential, it is crucial to generate a diverse and physically meaningful data set that spans a wide range of atomic configurations. For this purpose, we performed first-principles molecular dynamics (MD) simulations based on density functional theory to obtain total energies and atomic forces over multiple thermodynamic conditions. All simulations were carried out using the CP2K program[40] with the Quickstep module.[41] The temperature was varied between 298 and 700 K in 100 K increments to ensure coverage of both near-equilibrium and thermally activated configurations, effectively sampling the configurational space expected during finite-temperature simulations. Trajectories were recorded at sufficiently long time intervals to capture both short-range vibrations and larger-scale framework distortions, ensuring comprehensive sampling of local environments relevant to Li-ion diffusion.

The exchange−correlation energy was described within the generalized gradient approximation (GGA) using the Perdew−Burke−Ernzerhof (PBE) functional.[42] Long-range dispersion interactions, which are critical for describing van der Waals forces within the porous ZIF framework, were accounted for using Grimme's D3

https://doi.org/10.1021/acsami.6c03442
ACS Appl. Mater. Interfaces XXXX, XXX, XXX−XXX

correction.[43] Core electrons were represented by Goedecker−Teter−Hutter (GTH) pseudopotentials,[44,45] while the valence electrons were treated with a short-range, molecularly optimized double-ζ valence plus polarization (DZVP) basis set. To ensure reliable convergence of the electrostatic energy, an energy cutoff of 500 Ry was applied for the auxiliary plane-wave expansion of the charge density. The Born−Oppenheimer *ab initio* molecular dynamics simulations were performed with an integration time step of 1.0 fs. Both the pure Co and Zn/Co-mixed ZIF-62 systems were equilibrated in the isothermal−isobaric (NpT) ensemble at 1 bar, employing a Parrinello−Rahman barostat[46] with a time constant of 500 fs to maintain pressure stability. Temperature control was achieved using a chain of six Nosé−Hoover thermostats,[47] each with a 100 fs time constant, allowing accurate sampling of the canonical ensemble. The total length of the trajectory for each system was 15 ps.

From these AIMD trajectories, we extracted a large and diverse set of configurations suitable for training the deep neural network (DNN) potential. Specifically, 3654 configurations were obtained for the pure Co−ZIF-62 system, containing 416 atoms (C: 140, H: 112, N: 70, F: 36, O: 24, Co: 16, S: 12, Li: 6). For the Zn/Co-mixed ZIF-62 structure, 4312 configurations were collected, also comprising 416 atoms (C: 140, H: 112, N: 70, F: 36, O: 24, Co: 10, Zn: 6, S: 12, Li: 6). This comprehensive data set spans the relevant thermodynamic states and local atomic environments, forming a rigorous foundation for training a DNN potential that can accurately describe the structural and dynamic behavior of Li-doped ZIF-62 glasses.

2.2. Training and Validation of Deep Neural Network Potentials

Building upon the extensive first-principles molecular dynamics data set, a deep learning−based force field was developed using the DeePMD-kit package.[48,49] The primary objective of this step was to construct a transferable and data-efficient interatomic potential capable of reproducing the structural and dynamical characteristics of the ZIF-62 frameworks across a broad thermodynamic range. Previously, DNN potentials have been reported for MOF systems. For example, DNNs have been developed to study both crystalline and noncrystalline phases of ZIF-4,[50] as well as for the effective evaluation of Al-soc-MOF-1d in the context of H_2 adsorption.[51] These studies demonstrate that DNN potentials can achieve high accuracy with training data sets comprising thousands of configurations, yielding energy and force errors comparable to those of first-principles calculations while enabling simulations at significantly reduced computational cost. The training data set incorporated two distinct components to ensure both diversity and representativeness of the underlying potential-energy surface: (i) the initial data set, consisting of AIMD trajectories and single-point energy calculations of crystalline configurations sampled at regular time intervals, which provided a balanced description of equilibrium and thermally perturbed structures; and (ii) an extended data set, iteratively enriched through single-point DFT calculations selected via the active-learning protocol implemented in the DP-GEN package.[52] This iterative refinement strategy enabled the model to systematically identify and learn from configurations where its predictions exhibited higher uncertainty, thereby expanding its coverage of the configurational space in a self-consistent manner.

The neural network architecture followed a widely adopted hybrid ResNet-based framework.[53,54] The embedding network consisted of three layers, each containing 25, 50, and 100 neurons, respectively, which transformed the raw atomic environment descriptors into a continuous latent representation. This representation was then mapped to atomic energies through a fitting network consisting of three layers, each with 240 neurons. The "se_e2_a" descriptor[55] was chosen as it provides an efficient many-body representation of the local atomic environment. In this approach, the embedding network uses the interatomic distances between a central atom and its neighboring atoms as input. The resulting descriptor incorporates radial and angular information from the entire neighbor environment via symmetry-preserving transformations, thereby capturing the local geometry of the ZIF framework. Model training was performed for 6,000,000 iterations, with the loss function incorporating weighted contributions from total energies and atomic forces to ensure balanced learning of energetic and dynamical features. The learning rate was decayed exponentially from 1×10^{-3} to 3.51×10^{-8}, allowing for rapid early convergence followed by fine-tuning of the potential surface.

To rigorously validate the accuracy and stability of the converged DNN potential, long−time-scale molecular dynamics simulations were carried out using LAMMPS[56] interfaced with DeePMD-kit.[49] In these simulations, the trained DNN model served as a pair-style potential for on-the-fly evaluation of atomic energies and forces, thereby replicating the underlying chemistry of the reference AIMD data while enabling simulations over much longer time and length scales. For each production run, atomic trajectories were propagated using one of the four independently trained models generated in the initial training step, while the instantaneous forces on each atom were concurrently predicted by all four models. The degree of model convergence and internal consistency were quantified by the maximum standard deviation of predicted atomic forces, calculated as $\zeta = \max_i \langle |\mathbf{F}_i - \overline{\mathbf{F}}_i|^2 \rangle$, where $\mathbf{F}_i$ is the force on atom i from a single model and $\overline{\mathbf{F}}_i$ is the ensemble-averaged force over the four models. Configurations exhibiting high force deviations ($\zeta > 1.0$ eV/Å) were flagged as poorly represented regions of configuration space. These snapshots were recalculated at the DFT level to obtain reference energies (E) and atomic forces ($\mathbf{F}_i$), which were then appended to the training data set. The DNN potential was retrained with this augmented data set, thereby completing one active-learning cycle. This iterative process was repeated until the fraction of configurations exceeding the threshold ($\zeta > 1.0$ eV/Å) dropped below 0.01% of the total sampled configurations, indicating satisfactory convergence and comprehensive sampling of the relevant potential-energy landscape.

2.3. Li-Ion Transport Simulations Using Deep Neural Network Potentials

To quantitatively assess lithium-ion transport in both pure and mixed-metal ZIF-62 systems, large-scale MD simulations were performed using the fully converged DNN potential trained in the preceding section. Starting from equilibrated configurations, $2 \times 2 \times 2$ supercells were constructed for both pure and mixed-metal nodes, with box lengths of a = 30.8742 Å, b = 31.2834 Å, and c = 36.3436 Å, and all angles equal to 90°. The considered size of supercell helps to minimize finite-size effects and to ensure statistically meaningful sampling of ion migration pathways, resulting in a total of 3328 atoms per simulation cell. The Co/(Co + Zn) ratios were systematically varied as 0.25, 0.50, 0.625, 0.75, and 1.00 to probe the compositional dependence of Li-ion mobility across the mixed-metal series.

Each supercell was subjected to DPMD simulations, wherein the DNN potential—accurately reproducing the underlying DFT-level potential energy surface—was used to evaluate atomic forces and energies at every integration step. Prior to production, the systems were equilibrated in the isothermal−isobaric (NpT) ensemble at 450 K, allowing both temperature stabilization and cell-volume relaxation to remove any residual stress in the amorphous framework. After equilibration, the box lengths showed only minor variations from the initial values (Table S1). This equilibration step ensured that the simulated structures faithfully represent thermally equilibrated glassy configurations under realistic conditions. Subsequently, long-time scale production runs were conducted in the canonical (NVT) ensemble for up to 3 ns to capture the full range of Li-ion dynamical processes—from localized vibrations and cage-to-cage hopping to long-range diffusion. We carefully monitored the equilibration and stability of key thermodynamic quantities, including temperature, pressure, volume, and total energy, to ensure that the system reached equilibrium within 3 ns. The simulation duration and system size together provide an adequate statistical basis for computing ionic conductivities and activation energies while preserving the local structural integrity of the framework. This integrated DPMD workflow thus bridges atomistic-level dynamics with macroscopic transport behavior, offering quantitative insight into how metal-node substitution modulates the Li-ion conduction network within ZIF-62 glasses.

https://doi.org/10.1021/acsami.6c03442
ACS Appl. Mater. Interfaces XXXX, XXX, XXX−XXX

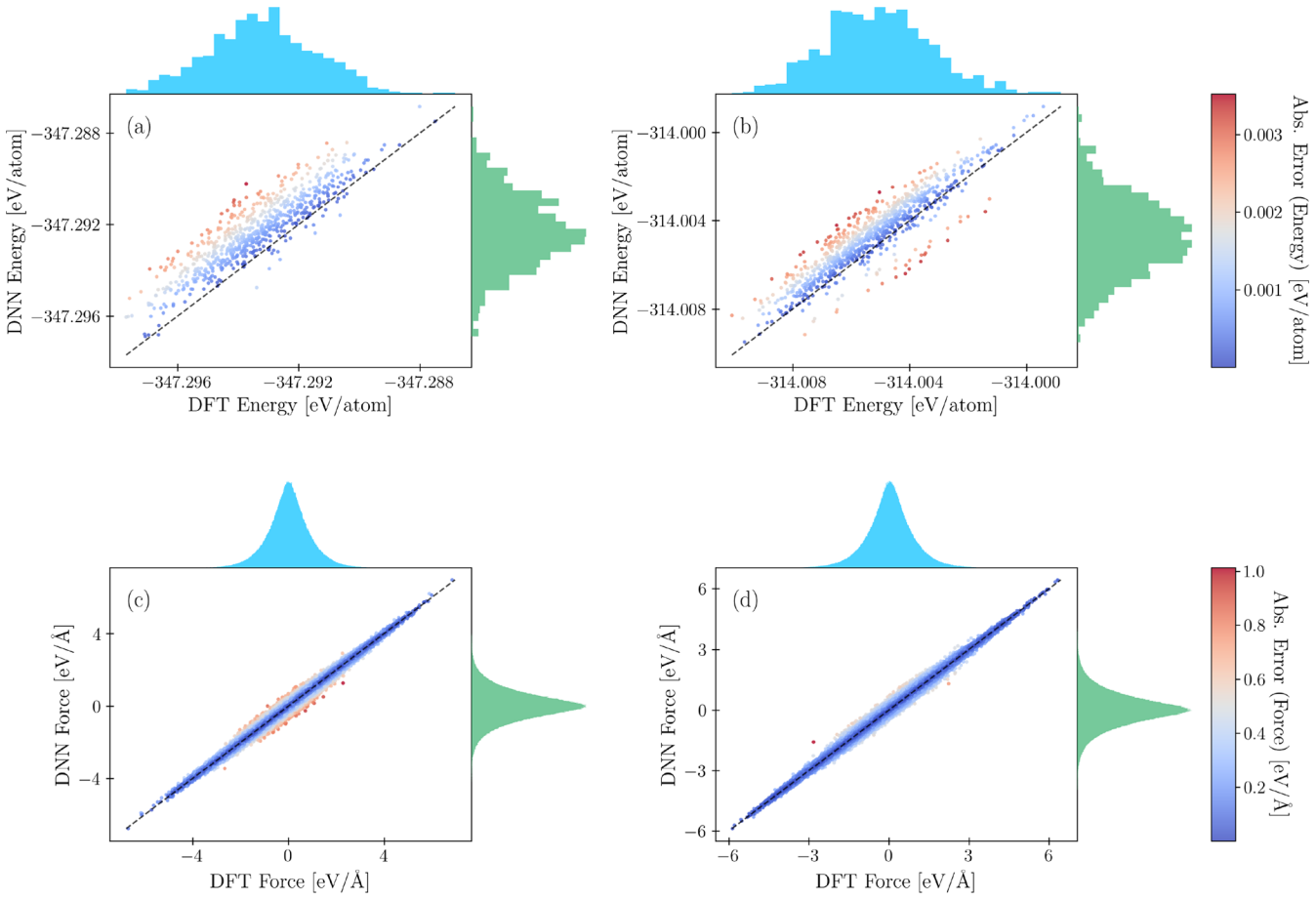

Figure 1. Comparison between DFT reference data and DNN predictions for ZIF-62 systems. Top row: total energies for (a) pure and (b) mixed-metal frameworks. Bottom row: atomic forces for (c) pure and (d) mixed-metal frameworks. Histograms along the axes show the distributions of predicted values, while color bars represent absolute deviations, demonstrating excellent agreement between DFT and DNN results.

3. RESULTS AND DISCUSSION

3.1. Accuracy and Reliability of the Deep Neural Network Potential

A prerequisite for any meaningful discussion of Li-ion transport in structurally complex, mixed-metal ZIF-62 glasses is the availability of an interatomic potential that faithfully captures both the energetics and local forces governing framework flexibility and ion dynamics. We therefore begin by assessing the accuracy and robustness of the DNN potential developed in this work, which serves as the foundation for all subsequent large-scale molecular dynamics simulations. The DNN potential was trained by minimizing a composite loss function (L), defined as a weighted sum of the squared deviations in total energies and atomic forces between the reference DFT data and the DNN predictions

$$L = p_e \Delta E^2 + \frac{p_f}{3N} \sum_i \Delta F_i^2 \quad (1)$$

where ΔE^2 and ΔF_i^2 represent the squared errors in the system energy and the component-wise atomic forces for a system containing N atoms. The prefactors p_e and p_f control the relative importance of energy and force matching during training. In line with standard practice for DeepMD models, these weights were gradually adjusted to emphasize force accuracy at early stages, and energy consistency at later stages, with p_e increased from 0.2 to 8 and p_f decreased from 1000 to 1 over the course of training.

The learning curves of the final DNN models for both pure and mixed-metal ZIF-62 systems are shown in Figure S1. In both cases, the loss associated with energies and forces decreases smoothly with the number of training iterations, indicating stable convergence without signs of overfitting. After approximately 1×10^6 training steps, the DNN achieved energy fitting errors of $\sim 9 \times 10^{-6}$ eV and $\sim 6 \times 10^{-6}$ eV for the 1.00−ZIF-62 and 0.625−ZIF-62 systems, respectively. The corresponding force errors were $\sim 6 \times 10^{-2}$ eV Å^{-1} and $\sim 5 \times 10^{-2}$ eV Å^{-1}. These values fall well within the accuracy range typically reported for DPMD models applied to chemically complex frameworks and disordered materials,[51,57,58] confirming that the trained potential can reliably reproduce DFT-level forces that are critical for ion transport dynamics.

Beyond the initial training, the accuracy of the model was systematically improved through successive DP-GEN active-learning iterations, in which configurations exhibiting considerable force uncertainty were identified and incorporated into the training data set. This iterative refinement is reflected in the progressive reduction of the maximum standard deviation of atomic forces (ζ) across four independently trained DNN models, indicating a shrinking region of poorly represented configurational space. Such convergence is significant for glassy MOFs, where subtle variations in local coordination environments and framework distortions can strongly influence ion migration pathways. A more stringent validation of the trained DNN potential is provided by a direct comparison of DNN-

https://doi.org/10.1021/acsami.6c03442
ACS Appl. Mater. Interfaces XXXX, XXX, XXX−XXX

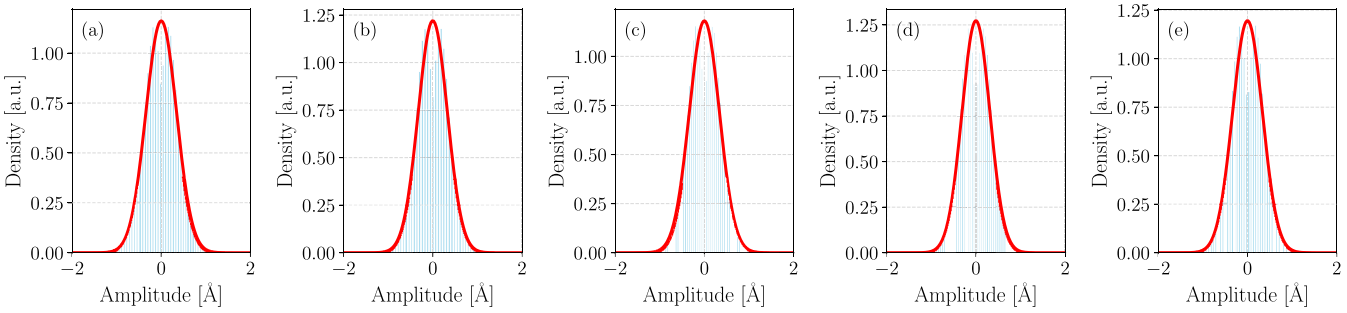

Figure 2. Distributions of vibrational amplitudes of Li^+ ions in ZIF-62 at 450 K for different Co/(Co + Zn) ratios: (a) 1.00, (b) 0.25, (c) 0.50, (d) 0.625, and (e) 0.75. Vibrational amplitudes are computed from Li^+ trajectories over the full production run following equilibration. The histograms represent displacements within metastable sites, defined as high-occupancy regions identified using the time-averaged occupancy grid (TAOG) method, corresponding to dynamically stable Li-ion positions. Solid red lines denote Gaussian fits, while displacements exceeding ~1 Å indicate hopping events between adjacent sites.

predicted energies and forces with DFT reference values for an independent test set, as shown in Figure 1. For the pure Co−ZIF-62 system, the root-mean-square error (RMSE) in energies is 0.0014 eV/atom, while the mixed-metal ZIF-62 system exhibits an even lower RMSE of 0.001 eV/atom. The corresponding force RMSE values are 0.0860 eV $Å^{-1}$ and 0.0714 eV $Å^{-1}$ for the pure and mixed systems, respectively. The narrow distributions and the near-linear correlation between DFT and DNN predictions demonstrate that the model accurately captures both energetic trends and force fluctuations across chemically distinct metal-node environments.

Taken together, these results demonstrate that the present DNN potential achieves near-DFT accuracy for both pure and mixed-metal ZIF-62 systems, while enabling simulations at length and time scales inaccessible to first-principles methods. This level of fidelity is essential for the subsequent analysis of Li-ion transport, where subtle differences in local framework flexibility and ion−framework interactions ultimately dictate diffusion mechanisms and ionic conductivity.

3.2. Li-Ion Transport Mechanisms in Mixed-Metal ZIF-62

Having established the accuracy and transferability of the DNN potential, we now employ it to elucidate the microscopic mechanisms governing Li-ion transport in pure and mixed-metal ZIF-62 frameworks. DPMD simulations were carried out on 2 × 2 × 2 supercells with Co/(Co + Zn) ratios of 0.25, 0.50, 0.625, 0.75, and 1.00 under identical thermodynamic conditions to those used during potential training. All simulations were performed at 450 K and extended to 3 ns, allowing Li-ion migration to be sampled over time scales relevant to activated diffusion in glassy MOF electrolytes. Notably, at 450 K, ZIF-62 (with both single and mixed metal compositions) exhibits a moderate degree of structural disorder, consistent with previous experimental studies on ZIF-62 glasses, which report diminished Bragg peaks in X-ray diffraction (XRD) and broadened features in NMR spectra.[39,59] Despite this loss of long-range order, the organic linkers remain structurally intact, thereby preserving the local framework connectivity and providing a basis for the observed lithium-ion displacement behavior.

In solid-state ionic conductors such as crystalline or glassy MOFs, Li-ion transport does not proceed via simple, uncorrelated hops but instead emerges from a complex interplay between local structural disorder, framework flexibility, and collective atomic motions.[60,61] In such systems, ion migration is often facilitated by transient distortions of the host lattice, correlated jumps, and anharmonic vibrations that dynamically reshape the local energy landscape. MD simulations are uniquely suited to capture these coupled effects, as they explicitly account for both ionic motion and framework response. This capability stands in contrast to static approaches—such as nudged elastic band calculations—which provide valuable information on isolated migration barriers but cannot fully describe the time-dependent fluctuations and cooperative phenomena inherent to disordered materials. Rather than limiting the analysis to tracer diffusivities or Arrhenius activation energies, a trajectory-based treatment enables access to a richer set of transport descriptors, including jump frequencies, vibrational amplitudes, site occupancies, correlation factors, and collective motions.[62] Among these, the vibrational dynamics of Li ions within metastable sites play a central role in determining the likelihood of successful hopping events and, ultimately, macroscopic ionic conductivity.

At the atomistic level, Li ions spend the majority of their time undergoing localized vibrational motion within the potential well-defined by neighboring framework atoms. Only sporadically do they acquire sufficient thermal energy to overcome the local migration barrier and transition to an adjacent site. The characteristic frequency of these localized oscillations can be interpreted as an attempt frequency $\nu_{attempt}$, which sets the prefactor for thermally activated hopping processes. Importantly, $\nu_{attempt}$ is not an independent quantity but is often correlated with the activation energy, a relationship commonly referred to as the Meyer−Neldel rule.[63] In disordered solids, higher activation barriers are frequently accompanied by higher attempt frequencies due to increased vibrational entropy near the transition state. The present DPMD-based analysis naturally captures these effects by explicitly resolving the localized, anharmonic vibrations of Li ions within their chemically and topologically distinct environments. Unlike simplified harmonic models—where vibrational spectra are derived from normal modes at equilibrium and transition-state geometries—the present approach incorporates the influence of local strain fields, framework flexibility, and dynamic disorder arising from mixed-metal coordination. This is particularly critical for glassy or compositionally heterogeneous MOFs, where local environments deviate substantially from idealized crystalline motifs and where transport pathways are continuously reshaped by thermal fluctuations.

Figure 2 presents the distributions of Li-ion vibrational amplitudes for pure and mixed-metal ZIF-62 systems at 450 K. The displacement histograms, fitted with Gaussian functions, provide a quantitative measure of the average vibrational amplitude associated with Li ions residing in metastable hopping

https://doi.org/10.1021/acsami.6c03442
ACS Appl. Mater. Interfaces XXXX, XXX, XXX−XXX

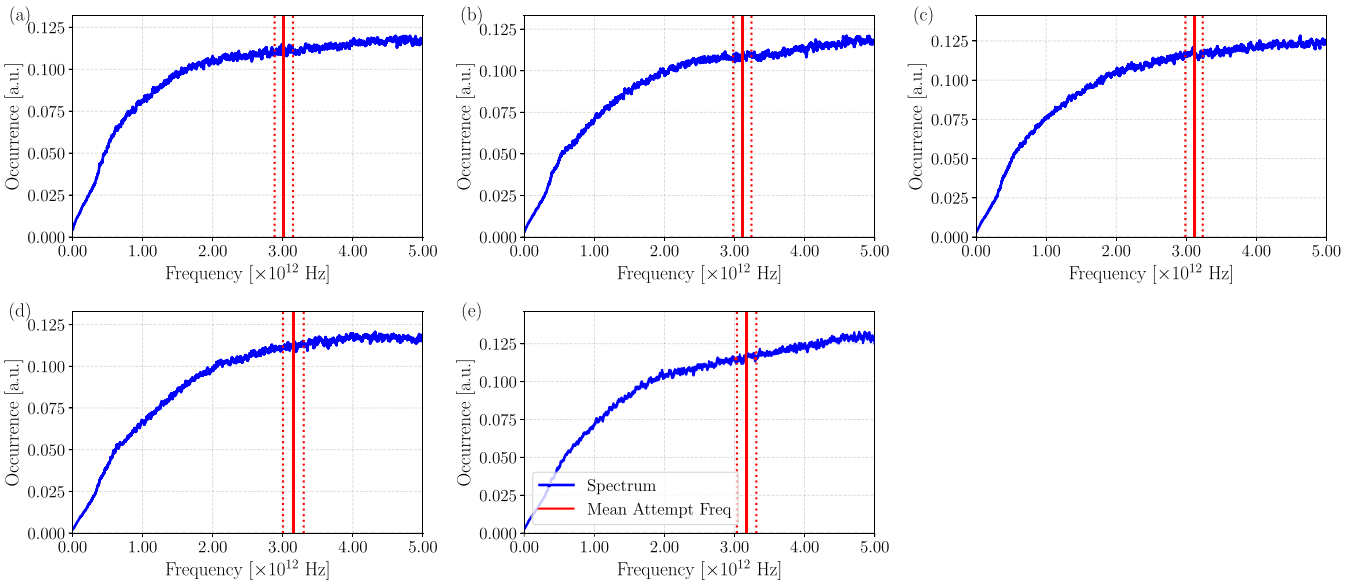

Figure 3. Vibrational frequency spectra of diffusing Li ions in ZIF-62 at 450 K for different Co/(Co + Zn) ratios: (a) 1.00, (b) 0.25, (c) 0.50, (d) 0.625, and (e) 0.75. Solid red lines denote the average vibrational (attempt) frequency, while dotted red lines indicate one standard deviation, highlighting the narrow distribution of vibrational time scales across compositions.

sites. Across all compositions, the majority of vibrational displacements are confined within a narrow range, indicating well-defined local potential wells. A small fraction of displacements exceeding 1 Å is observed in all systems and can be attributed to successful hopping events between adjacent sites rather than purely vibrational motion. The standard deviations extracted from Gaussian fitting (summarized in Table S2) show that the $\pm 2\sigma$ range spans approximately 0.606−0.676 Å, implying that Li ions remain localized near their metastable sites for roughly 95% of the simulation time. Notably, the 0.50−ZIF-62 composition exhibits the largest vibrational amplitude (0.676 Å), suggesting enhanced local flexibility and a broader distribution of accessible configurations. This increased vibrational freedom is expected to raise the attempt frequency and, in turn, promote more frequent hopping events—an effect that foreshadows the compositional trends in Li-ion diffusivity discussed in subsequent sections.

The composition-dependent broadening of the vibrational-amplitude distributions therefore points to systematic changes in the local curvature of the Li-ion potential wells and, by extension, in the vibrational time scales that govern hopping attempts. Larger vibrational excursions reflect softer local environments and enhanced framework flexibility, which are expected to manifest as shifts in the characteristic vibrational frequencies of Li ions. To quantify this connection and directly assess how metal substitution modulates the attempt frequency underlying Li-ion hopping, we next analyze the vibrational frequency spectra extracted from the DPMD trajectories.

Figure 3 presents the vibrational frequency spectra of diffusing Li ions in ZIF-62 at 450 K for different Co/(Co + Zn) ratios, with the corresponding statistical descriptors summarized in Table S2. The distributions were obtained from the time-resolved Li-ion trajectories and provide a direct measure of the attempt frequency associated with localized vibrational motion prior to hopping events. Across all compositions, the average vibrational frequencies fall within a narrow window of 3.01−3.11 × 10^{12} s^{-1}, indicating that Li-ion dynamics in ZIF-62 are governed by a well-defined vibrational time scale that is only weakly perturbed by metal substitution. These values are in excellent agreement with prior AIMD-based studies of ionic transport in solid electrolytes, which typically report attempt frequencies in the range of 10^{12}−10^{13} Hz.[62,64] Comparable magnitudes have also been reported for oxide-ion conductors, such as Sm-doped ceria, where phonon-based analyses yielded attempt frequencies of 1.47 × 10^{12} s^{-1} under the harmonic approximation at constant volume and 7.67 × 10^{12} s^{-1} under the quasi-harmonic approximation at constant pressure.[65] The close correspondence between these values and those obtained here underscores the physical realism of the present DPMD framework and supports the reliability of the extracted dynamical descriptors.

Importantly, when interpreted in conjunction with the vibrational-amplitude analysis, the relatively modest variation in average vibrational frequency suggests that composition-dependent changes in Li-ion transport are not driven by large shifts in the fundamental attempt frequency. Instead, they are more likely governed by variations in the distribution of local environments, barrier heights, and the probability of successful barrier crossing—effects that will become evident when the hopping statistics, mean-squared displacements, and tracer diffusivities are examined in the following discussion.

Because LiTFSI molecules are initially introduced at random positions within the ZIF-62 framework, the resulting Li-ion trajectories do not conform to any predefined lattice symmetry or known crystallographic site topology. As a consequence, conventional site-identification approaches based on static structure or symmetry analysis are not applicable. To address this challenge, we employ the time-averaged occupancy grid (TAOG) method—a density-based, assumption-free approach that has been successfully applied to identify ion sites in both crystalline and amorphous solid electrolytes.[66−68] This methodology enables the direct extraction of preferred ion locations solely from dynamical information, without requiring prior knowledge of site geometry or connectivity.

In the TAOG framework, the simulation cell is discretized into a fine three-dimensional grid of volumetric elements (voxels). At each time step of the molecular-dynamics trajectory, the instantaneous positions of all mobile Li ions are mapped

https://doi.org/10.1021/acsami.6c03442
ACS Appl. Mater. Interfaces XXXX, XXX, XXX−XXX

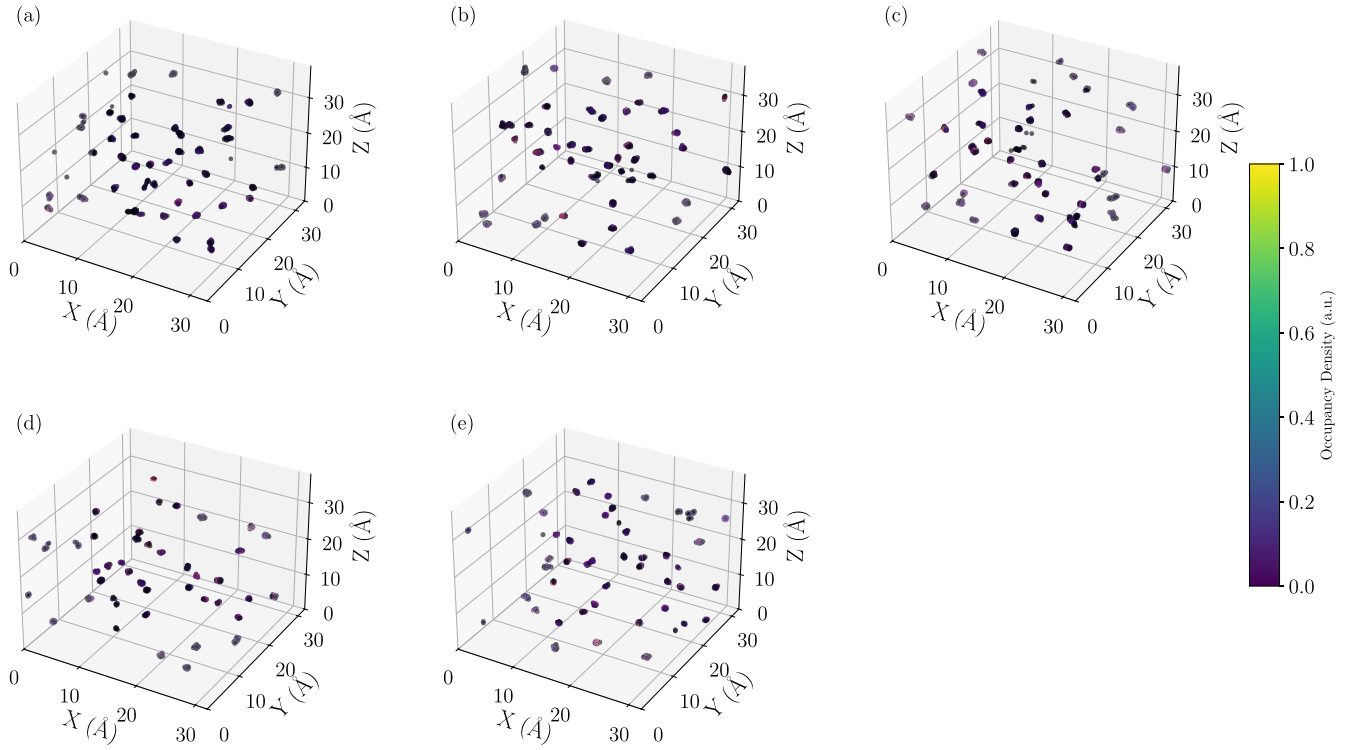

Figure 4. Time-averaged occupancy grid (TAOG) maps showing the spatial distribution of Li-ion occupation sites in a 2 × 2 × 2 ZIF-62 supercell at 450 K for Co/(Co + Zn) ratios of (a) 1.00, (b) 0.25, (c) 0.50, (d) 0.625, and (e) 0.75. High-density regions correspond to metastable Li-ion sites identified from the DPMD trajectories.

onto this grid. By accumulating voxel occupancies over the full simulation time, a three-dimensional probability density distribution is obtained that reflects the spatial residence time of Li ions within the framework. Regions of high probability density correspond to locations where Li ions spend a significant fraction of time and therefore represent energetically favorable metastable sites. Importantly, this approach captures both well-defined sites and more diffuse occupation regions that emerge from local structural disorder, making it particularly well-suited for glassy or compositionally heterogeneous MOF systems. The TAOG-derived spatial distributions of Li-ion occupation sites for the different Co/(Co + Zn) ratios are shown in Figure 4. Across the compositional series, the 0.25, 0.50, 0.65, 0.75, and 1.0 ZIF-62 systems exhibit approximately 57, 55, 48, 48, and 73 distinct high-probability occupation sites, respectively. These sites correspond to metastable, low-energy positions resulting from the interplay between the local coordination environment of the ZIF cages, the presence of mixed-metal nodes, and electrostatic interactions with the $TFSI^-$ anions. Notably, the variation in the number of identified sites does not exhibit a direct one-to-one correlation with enhanced Li-ion transport. While a larger number of metastable sites increases the configurational space accessible to Li ions, efficient ionic conduction depends critically on additional factors, including the spatial connectivity between sites, the distribution of energy barriers separating them, and the dynamic response of the host framework. In particular, closely spaced but poorly connected sites may act as traps, whereas a smaller number of well-connected sites linked by low-barrier pathways can facilitate long-range diffusion.

To further elucidate the microscopic origin of Li-ion mobility in ZIF-62, we analyze the statistics of atomic displacements and their temporal evolution at 450 K for all compositions considered. While vibrational amplitudes and attempt frequencies characterize localized motion within metastable sites, displacement analysis directly captures the occurrence of rare but critical hopping events that enable long-range ion transport. Figure 5 presents the distribution of Li-ion displacement magnitudes accumulated over the simulation trajectories. Across both pure and mixed-metal ZIF-62 systems, the vast majority of displacements remain below 1 Å, which is significantly smaller than a typical interatomic distance. This behavior is consistent with Li ions spending most of their time undergoing localized vibrational motion within potential wells, as discussed in the preceding sections. The long tails observed in the displacement distributions correspond to infrequent but decisive hopping events between distinct metastable sites identified through the TAOG analysis.

Additional insight is obtained by examining the temporal evolution of individual Li-ion displacements, as shown in Figure 6. At early times, Li ions predominantly oscillate around their initial equilibrium positions, reflecting confinement within local coordination environments. As the simulations progress, a subset of ions undergoes abrupt changes in position, signaling transitions to new metastable sites, after which they again exhibit localized vibrational motion. This characteristic step-like behavior is a hallmark of hopping-mediated diffusion in solid-state electrolytes. The extent and frequency of such hopping events vary markedly with composition. In the pure ZIF-62 system, six Li ions display maximum displacements of approximately 4 Å, indicative of transitions between nearby sites within the framework. In contrast, the 0.25-ZIF composition exhibits more pronounced displacements, with one ion traveling nearly 6 Å, another about 5 Å, and a third around 4 Å, alongside several ions showing intermediate displacements of approximately 1.5 Å. An even more substantial

https://doi.org/10.1021/acsami.6c03442
ACS Appl. Mater. Interfaces XXXX, XXX, XXX−XXX

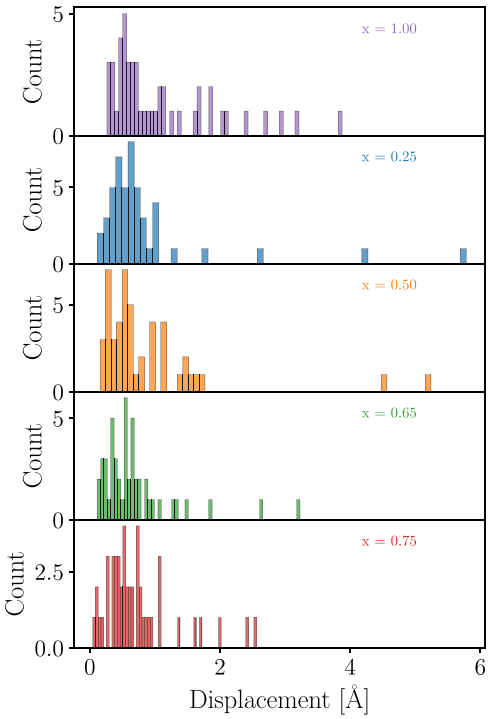

Figure 5. Displacement distributions of diffusing Li ions in ZIF-62 at 450 K for different Co/(Co + Zn) compositions (indicated by x). Short displacements correspond to localized vibrational motion, while long tails indicate rare hopping events between metastable sites.

effect is observed for the 0.50-ZIF composition, where the largest displacements reach ~5.5 Å and ~4.5 Å, accompanied by multiple ions undergoing displacements of around 2.5 Å. These large excursions are indicative of enhanced site-to-site connectivity and reduced effective barriers for long-range transport. By comparison, the 0.65- and 0.75-ZIF systems exhibit more restricted motion. In these compositions, the maximum displacements are limited to approximately 3 Å and 2.75 Å, respectively, with the remaining ions displaying smaller amplitudes in the range of 1.5−2 Å. This reduction in displacement magnitude suggests a progressively more constrained transport landscape as the system moves away from the optimally mixed-metal regime. These trends indicate that Li^+ transport in the Zn-rich 0.25 composition is hindered by insufficient network connectivity arising from structural heterogeneity, whereas the Co-rich 0.75 system is limited by a stronger coordination environment that enhances framework rigidity around Li sites and increases the barriers for site-to-site transitions. In contrast, the 0.50 composition achieves an optimal balance between flexibility and structural integrity, in which mixed Zn/Co nodes, together with benzimidazolate linkers, facilitate the formation of interconnected, low-barrier pathways for Li^+ transport.

Collectively, these results demonstrate that the 0.50-ZIF composition supports the largest average Li-ion displacements and the most frequent long-range hopping events. This behavior reflects an optimal balance between structural disorder and framework flexibility introduced by partial metal substitution. Such substitution modifies the local coordination environment and induces subtle lattice distortions that facilitate Li-ion migration through hopping into neighboring metastable sites or transient vacancies. When combined with the vibrational and site-occupancy analyses discussed earlier, the displacement statistics provide compelling evidence that mixed-metal ZIF-62 frameworks—particularly at intermediate Co/Zn ratios—offer a uniquely favorable energy landscape for Li-ion transport.

Further insight into Li-ion transport is obtained from the van Hove correlation functions, which resolve both individual-ion displacements and the persistence of the local ionic environment. The self-part, $G_{self}(r, t)$, directly reflects Li-ion displacement statistics, while the distinct part, $G_{distinct}(r, t)$, captures the stability of the surrounding Li-ion cage. At low Co fractions [Co/(Co + Zn) = 0.25−0.50], $G_{self}(r, t)$ develops pronounced shoulders at larger r with increasing time (shown in Figure S2), indicating frequent long-range hopping events and a broad distribution of Li displacements. This behavior is consistent with the large vibrational amplitudes and displacement statistics observed for these compositions, reflecting a highly connected network of accessible hopping pathways. With increasing Co content [Co/(Co + Zn) = 0.65−0.75 and Co-rich ZIF-62], the decay of $G_{self}(r, t)$ becomes steeper, and the distributions terminate at smaller distances, signaling increasingly localized motion and suppressed long-range hops. In contrast, $G_{distinct}(r, t)$ exhibits similar features across all compositions (shown in Figure S3), with a strong first peak near the Li−Li nearest-neighbor distance and a persistent second-shell feature. The near invariance of peak positions with time indicates that Li ions predominantly exchange positions within comparable local environments, rather than inducing substantial rearrangements of the Li sublattice. The smooth evolution of $G_{distinct}(r, t)$ with composition thus suggests that the observed changes in Li-ion transport arise primarily from modifications in hopping connectivity and residence times, rather than from significant changes in static Li−Li packing or cage geometry.

Building on the identification of metastable Li-ion sites and the composition-dependent hopping behavior revealed by the

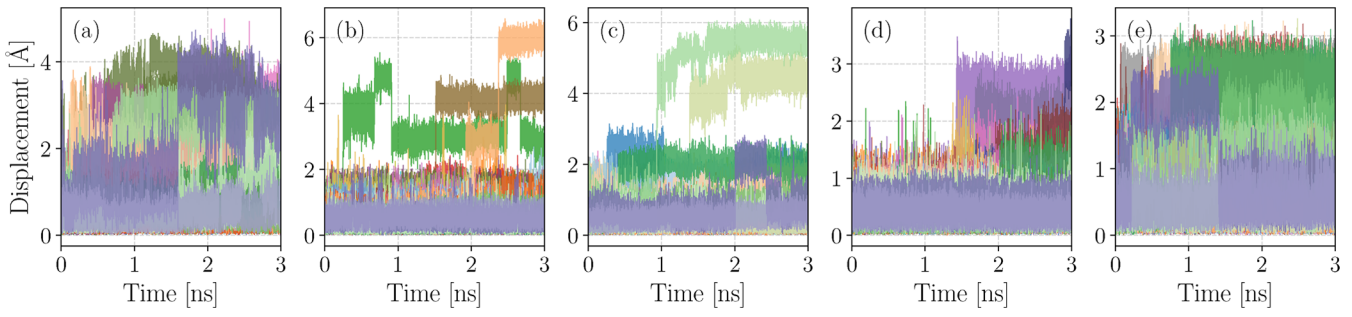

Figure 6. Time evolution of individual Li-ion displacements in ZIF-62 at 450 K for varying Co/(Co + Zn) ratios: (a) 1.00, (b) 0.25, (c) 0.50, (d) 0.625, and (e) 0.75. Step-like increases in displacement reflect site-to-site hopping events followed by localized vibrational motion.

https://doi.org/10.1021/acsami.6c03442
ACS Appl. Mater. Interfaces XXXX, XXX, XXX−XXX

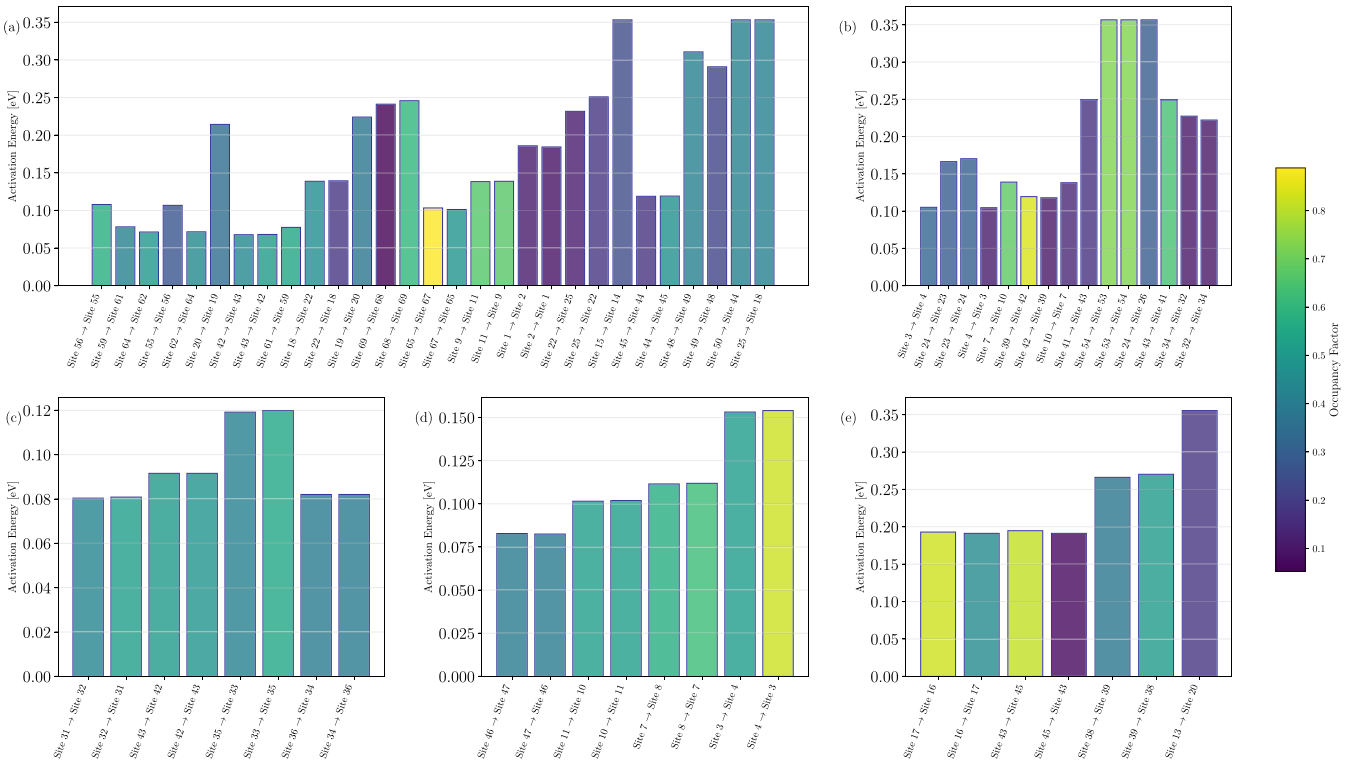

Figure 7. Distribution of activation energy barriers for Li-ion hopping events in ZIF-62 at 450 K for different Co/(Co + Zn) compositions: (a) 1.00, (b) 0.25, (c) 0.50, (d) 0.65, and (e) 0.75. Each data point corresponds to an effective activation energy extracted from jump statistics, highlighting the heterogeneous migration landscape and composition-dependent barrier distributions.

displacement and TAOG analyses, we now quantify Li-ion transport in terms of elementary jump statistics. In disordered frameworks, such as glassy or partially amorphous MOFs, long-range diffusion emerges from a sequence of localized hops between transient occupation sites, rather than from motion along a periodic lattice. Accordingly, a jump-based formalism provides a natural and physically transparent description of ion transport in these systems. The average transition frequency between occupation sites is defined through the mean jump rate, $\Gamma_i = \frac{J_i}{Nt}$, where J_i is the total number of observed jumps between the ith pair of sites over the simulation time t, and N is the number of diffusing Li ions. This definition directly links microscopic hopping events extracted from atomistic trajectories to macroscopic transport coefficients. Using the computed jump rates, the jump-rate diffusivity D_J is evaluated via the Einstein−Smoluchowski relation[69]

$$D_J = \sum_i \frac{\Gamma_i a_i^2}{2d} \tag{2}$$

where a_i denotes the jump distance associated with jump type i, and d is the dimensionality of diffusion. Unlike tracer diffusivities obtained from mean-squared displacement analyses, D_J explicitly resolves the contributions of individual hopping pathways, allowing the role of jump length and frequency to be disentangled.

To further characterize the energetic landscape governing Li-ion migration, the activation energy associated with each jump type is determined from the effective jump frequency. By normalizing the observed jump frequency with respect to the occurrence factor, the activation energy for the ith jump is obtained as

$$E_{a,i} = -k_B T \ln\left(\frac{J_i}{tN_i\nu^*}\right) \tag{3}$$

where k_B is the Boltzmann constant, T is the absolute temperature, N_i is the number of diffusing atoms participating in jump type i, and ν^* is the attempt (prefactor) frequency. Importantly, this definition inherently incorporates both energetic and entropic contributions to ion migration, in contrast to nudged elastic band or bond-valence-based approaches, which typically probe only static minimum-energy pathways.

The resulting distribution of activation barriers for all accessible Li-ion hopping events at 450 K is shown in Figure 7. A striking feature across all compositions is the wide dispersion of migration barriers between different site pairs. This behavior reflects the intrinsically heterogeneous energy landscape of the MOF framework, which comprises large cages, flexible linkers, and dynamically evolving local environments in the presence of LiTFSI. Unlike crystalline inorganic electrolytes with well-defined hopping sites and uniform barriers, ZIF-62 exhibits a continuum of metastable sites with varying connectivity, leading to a broad spectrum of activation energies.

The composition dependence of this landscape is summarized quantitatively in Table 1, which reports the average activation energies, their ranges, jump-rate diffusivities, and corresponding ionic conductivities. Notably, the average activation energy does not directly correlate with the jump diffusivity D_J, as the latter is not normalized by occurrence factors and therefore remains sensitive to rare but long-distance hopping events. Among all investigated systems, the 0.50-ZIF composition stands out, exhibiting the lowest average activation energy of approximately 0.093 eV and a relatively narrow distribution of barriers. This

https://doi.org/10.1021/acsami.6c03442
ACS Appl. Mater. Interfaces XXXX, XXX, XXX−XXX

Table 1. Summary of Li-Ion Transport Parameters in ZIF-62 at 450 K for Different Co/(Co + Zn) Compositions, Including Average Activation Energies ($\overline{E}_a$) and Their Ranges, Jump-Rate Diffusivities (D_J), and Estimated Ionic Conductivities Derived from Jump Statistics and Arrhenius Analysis

comp.	$\overline{E}_a$ (eV)	$E_{a(range)}$ (eV)	D_J (cm^2/s)	$\sigma(T)$ (S/cm)
1.00	0.175 ± 0.092	0.068−0.353	1.270×10^{-6}	7.26×10^{-4}
0.25	0.205 ± 0.089	0.105−0.357	3.992×10^{-7}	3.35×10^{-4}
0.50	0.093 ± 0.016	0.080−0.120	9.843×10^{-7}	6.02×10^{-3}
0.65	0.112 ± 0.026	0.082−0.154	3.809×10^{-7}	3.69×10^{-3}
0.75	0.237 ± 0.058	0.191−0.355	7.456×10^{-8}	1.47×10^{-4}

result is fully consistent with the enhanced vibrational amplitudes, increased displacement statistics, and optimal site connectivity identified earlier, collectively pointing to a uniquely favorable transport landscape at this intermediate metal-mixing ratio. To connect the microscopic jump statistics to experimentally relevant observables, the ionic conductivity $\sigma(T)$ is estimated using the Arrhenius relation

$$\sigma(T) = \sigma_0 \exp\left(-\frac{\overline{E}_a}{k_B T}\right) \tag{4}$$

where σ_0 is the Arrhenius prefactor and $\overline{E}_a$ is the average activation energy for ionic conduction. While σ_0 is typically obtained from temperature-dependent experimental measurements, the present work focuses on extracting conductivity estimates directly from local jump statistics. Accordingly, the prefactors σ_0 were adopted for both crystalline and glassy phases from a previously reported Arrhenius analysis of Li^+-conducting Zn−ZIF-62,[59] ensuring consistency with experimentally characterized reference systems. Given the relatively weak variation of σ_0 compared to the exponential dependence of ionic conductivity on the activation energy ($\overline{E}_a$), this approximation does not affect the observed trends (shown in Tables 1 and S3), which are predominantly governed by variations in $\overline{E}_a$.

The resulting ionic conductivities, listed in Table 1, clearly identify the 0.50-ZIF composition as the most conductive system at 450 K, with $\sigma \approx 6.0 \times 10^{-3}$ S·cm^{-1}. This value exceeds those of both lower and higher Co/(Co + Zn) ratios, reinforcing the conclusion that partial metal substitution optimally balances structural disorder and framework flexibility to promote efficient Li-ion transport. To place our results in a broader experimental context, we note that reported ionic conductivities for MOF-based Li electrolytes typically lie in the 10^{-5}−10^{-4} S cm^{-1} range at ambient to moderately elevated temperatures. This behavior is exemplified by systems such as a ZIF-62 quasi-solid-state electrolyte, which exhibits an ionic conductivity of 3.89×10^{-4} S cm^{-1} at 30 °C,[37] a ZIF-62-glass/polymer composite with 7.13×10^{-5} S cm^{-1} at 50 °C,[19] and a Li-MOF electrolyte based on Mg_2(dobdc) (dobdc^{4-} = 1,4-dioxido-2,5-benzenedicarboxylate), which shows an ionic conductivity of 3.1×10^{-4} S cm^{-1} at room temperature.[70] The conductivities estimated in the present work at 450 K are therefore consistent with the expected thermally activated transport behavior, following an Arrhenius-type increase with temperature. While a direct quantitative comparison at 450 K is not currently feasible due to the absence of experimental data for Li-salt-doped MOF glasses under these conditions, the agreement in order of magnitude and in the temperature scaling supports the physical validity of our predictions. Finally, Figure 7 reveals a pronounced asymmetry between forward and backward activation energies for jumps between nominally equivalent site pairs A → B versus B → A. This asymmetry arises from rapid, temperature-driven fluctuations in local coordination environments and site occupancies, which continuously reshape the effective energy landscape on subpicosecond time scales. Such dynamic asymmetry is inherently inaccessible to macroscopic experimental probes but emerges naturally from atomistic simulations that explicitly resolve local structural rearrangements. Its presence further underscores the importance of treating ion transport in MOF-based electrolytes as a fundamentally dynamic, nonequilibrium process rather than as motion over a static potential-energy surface.

Beyond single-ion hopping, Li-ion diffusion can transiently perturb the local electrostatic and structural environment, leading to the short-lived formation and annihilation of local energy minima. Such fluctuations may influence nearby ions and give rise to correlated or collective hopping events over finite length and time scales. The extent to which these cooperative effects contribute to macroscopic transport depends sensitively on the local chemical composition and framework topology. Molecular dynamics simulations are uniquely suited to capture these time- and space-correlated ionic motions, which remain inaccessible to static or mean-field descriptions.

To quantify correlated Li-ion migration, Li−Li displacement correlations were evaluated within a cutoff distance of 10 Å, chosen to encompass the physically relevant interaction range associated with Coulombic coupling, site sharing, and framework-mediated lattice responses. In MOF-based electrolytes, such correlations are inherently short-ranged and typically confined within a single pore or linker domain, corresponding to distances of approximately 5−10 Å. Beyond this range, Li ions reside in separate cages or across insulating organic linkers, and their motions become dynamically uncorrelated. Including larger distances would therefore introduce statistical noise without adding physical insight. The 10 Å cutoff thus captures all meaningful cooperative dynamics while excluding spurious long-range coincidences. As shown in Figure 8, the pristine Co-rich system [Co/(Co + Zn) = 1.00] exhibits the highest fraction of correlated Li-ion jumps, followed by the 0.25-ZIF composition. In contrast, the 0.75-ZIF system shows nearly no correlated motion within the defined cutoff. Although occasional simultaneous Li jumps are observed at larger separations (≈16 Å) in this composition, these events are attributed to accidental temporal coincidences rather than genuine cooperative dynamics. Importantly, correlated displacements are

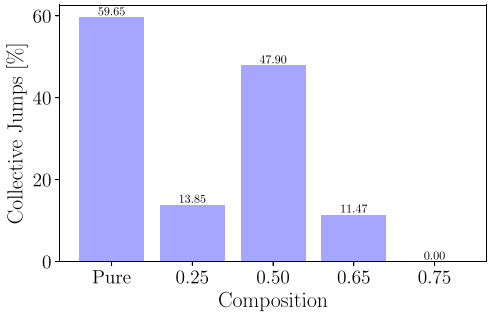

Figure 8. Fraction of correlated (collective) Li-ion hopping events as a function of Co/(Co + Zn) composition in ZIF-62, obtained from molecular dynamics simulations using a 10 Å spatial cutoff to identify cooperative motion.

https://doi.org/10.1021/acsami.6c03442
ACS Appl. Mater. Interfaces XXXX, XXX, XXX−XXX

confined to a short initial time window of approximately 3 ps, indicating that such events do not persist over time scales relevant to long-range diffusion. Additional statistical analysis of collective jump events (shown in Figure S4) further supports this picture. Across all compositions, collective migration is dominated by pairwise Li-ion jumps, with the highest occurrence in the pristine system and a reduced but noticeable contribution in the 0.50 mixed-metal composition. Events involving three Li ions are significantly less frequent and follow the same compositional trend. The fewer higher-order collective events highlights the limited spatial and temporal extent of cooperative motion in ZIF-62.

Although the pure system (1.0 ZIF-62) exhibits a greater number of metastable Li^+ sites (~73) than the 0.50 composition (~55), ionic conductivity is governed not by site count alone but by site connectivity, migration barriers, and framework dynamics. In the pure system, many metastable sites are spatially isolated or weakly connected, leading to Li^+ trapping and limited long-range diffusion. As reflected in Figure 7, Li^+ displacements are largely confined (typically up to ~4 Å), consistent with a relatively rigid framework that suppresses site-to-site transitions; correspondingly, the average activation barrier is higher (~0.175 eV). In contrast, the 0.50 composition exhibits a more interconnected network of metastable sites linked by low-energy pathways, with the lowest average activation barrier (~0.093 eV). The mixed-metal environment further creates a dynamically favorable energy landscape that balances site stability and mobility, enabling a percolating transport network. Consequently, despite having fewer metastable sites, the 0.50 system achieves higher ionic conductivity due to superior connectivity and reduced migration barriers.

Overall, these results demonstrate that Li-ion transport in ZIF-62 is primarily governed by the composition-dependent energy landscape and pore connectivity, rather than by sustained collective dynamics. While transient correlations do occur, they do not translate into long-lived cooperative transport and therefore have a negligible impact on long-time diffusivity. Instead, optimal ionic conductivity emerges from compositions that minimize migration barriers and promote continuous percolation pathways through the framework. This reinforces compositional tuning as a robust strategy for enhancing Li-ion transport in MOF-based electrolytes without relying on collective migration mechanisms.

4. CONCLUSION

A transferable deep neural network interatomic potential was developed using the DP-GEN framework and validated against DFT reference data, enabling accurate and efficient molecular dynamics simulations of Li-ion transport across pure and mixed-metal ZIF-62 compositions. The DNN potential faithfully captures both local framework distortions and long-range ion dynamics, providing access to transport mechanisms that are inaccessible to static or short-time scale first-principles approaches. DPMD simulations at 450 K reveal that Li-ion transport is dominated by localized vibrational motion within metastable cages, interspersed with thermally activated hopping events. Van Hove correlation analysis reveals that intermediate Co substitution [Co/(Co + Zn) ≈ 0.25−0.50] maximizes the spatial extent of Li displacements while maintaining a stable local coordination environment, indicating an optimal balance between framework flexibility and cage confinement.

Jump-resolved analysis further demonstrates that this dynamic regime produces the lowest effective activation barriers, with 0.50−ZIF-62 exhibiting a minimum average activation energy (~0.093 eV) and the highest ionic conductivity (~6.0×10^{-3} S·cm^{-1} at 450 K). Direction-dependent barriers and transient asymmetries underscore that ion migration occurs on a dynamically evolving energy landscape rather than a static potential surface. Correlated-motion analysis confirms that long-range diffusion proceeds predominantly via independent hopping events, with collective jumps being short-lived and negligible for macroscopic transport.

Overall, this work establishes a unified, DNN-enabled mechanistic picture in which optimal Li-ion conductivity in mixed-metal ZIF-62 arises from composition-tuned framework dynamics and hopping connectivity rather than sustained cooperative motion. These findings underscore the potential of machine-learning interatomic potentials for the predictive design of MOF-based solid-state electrolytes.

■ ASSOCIATED CONTENT

Data Availability Statement

The input files for the deep learning force field, the associated training data set, the trained machine-learning force field (MLFF), and example LAMMPS input scripts are available on GitHub at: GitHub repository.

Supporting Information

The Supporting Information is available free of charge at https://pubs.acs.org/doi/10.1021/acsami.6c03442.

Optimized simulation cell parameters for different compositions; Li-ion vibrational amplitudes, attempt frequencies, and Gaussian fit statistics; comparison of ionic conductivities for crystalline and glassy phases; DNN training convergence (learning curves); self-and distinct part of van Hove correlation functions; and statistical distribution of collective Li-ion hopping events, resolved by the number of ions participating in correlated jumps across different compositions (PDF)

■ AUTHOR INFORMATION

Corresponding Authors

Ram Sewak − *Department of Chemistry, Indian Institute of Technology Gandhinagar, Gandhinagar 382355 Gujarat, India;* orcid.org/0000-0001-5700-0122; Email: ram.sewak@iitgn.ac.in

Anirban Mondal − *Department of Chemistry, Indian Institute of Technology Gandhinagar, Gandhinagar 382355 Gujarat, India;* orcid.org/0000-0003-3029-8840; Email: amondal@iitgn.ac.in

Complete contact information is available at: https://pubs.acs.org/10.1021/acsami.6c03442

Author Contributions

R.S. and A.M. conceived the problem. R.S. conducted all the simulations. R.S. and A.M. analyzed the results and prepared the draft.

Notes

The authors declare no competing financial interest.

■ ACKNOWLEDGMENTS

The authors gratefully acknowledge the Indian Institute of Technology Gandhinagar, India, for providing research facilities

and financial support. We thank PARAM Ananta for computational resources.

REFERENCES

(1) Hasan, M.; Haque, R.; Jahirul, M.; Rasul, M.; Fattah, I.; Hassan, N.; Mofijur, M. Advancing energy storage: The future trajectory of lithium-ion battery technologies. *J. Energy Storage* **2025**, *120*, No. 116511.
(2) Yu, Y.; Hu, S.; Huang, J. Germanium-modified silicon as anodes in Si−Ge air batteries with enhanced properties. *J. Phys. Chem. Solids* **2021**, *157*, No. 110226.
(3) Wang, K.; Pei, S.; He, Z.; Huang, L.-a.; Zhu, S.; Guo, J.; Shao, H.; Wang, J. Synthesis of a novel porous silicon microsphere@carbon core-shell composite via in situ MOF coating for lithium ion battery anodes. *Chem. Eng. J.* **2019**, *356*, 272−281.
(4) Liu, W.; Cheng, P.; Yan, X.; Gou, H.; Zhang, S.; Shi, S. Facile One-Step Solution-Phase Route to Synthesize Hollow Nanoporous Cu_xO Microcages on 3D Copper Foam for Superior Li Storage. *ACS Sustainable Chem. Eng.* **2021**, *9*, 4363−4370.
(5) Yu, Y.; Hu, S.; Huang, J. Adsorption and diffusion of lithium and sodium on the silicon nanowire with substrate for energy storage application: A first principles study. *Mater. Chem. Phys.* **2020**, *253*, No. 123243.
(6) Dai, X.; Zhang, X.; Wen, J.; Wang, C.; Ma, X.; Yang, Y.; Huang, G.; Ye, H.-M.; Xu, S. Research progress on high-temperature resistant polymer separators for lithium-ion batteries. *Energy Storage Mater.* **2022**, *51*, 638−659.
(7) Liu, H.; Cheng, X.-B.; Huang, J.-Q.; Yuan, H.; Lu, Y.; Yan, C.; Zhu, G.-L.; Xu, R.; Zhao, C.-Z.; Hou, L.-P.; He, C.; Kaskel, S.; Zhang, Q. Controlling Dendrite Growth in Solid-State Electrolytes. *ACS Energy Lett.* **2020**, *5*, 833−843.
(8) Tariq, A.; Ali, G.; Waqas, U.; Ahmad, K. J.; Ramay, S. M.; Afzal, F.; Atiq, S. Synergistic integration of rGO into cobalt oxide matrix for efficient electrochemical performance mediated by structural stability. *J. Energy Storage* **2024**, *80*, No. 110346.
(9) Hou, J.; Ma, X.; Fu, J.; Vanaphuti, P.; Yao, Z.; Liu, Y.; Yang, Z.; Wang, Y. A green closed-loop process for selective recycling of lithium from spent lithium-ion batteries. *Green Chem.* **2022**, *24*, 7049−7060.
(10) Yan, C.; Zhang, X.-Q.; Huang, J.-Q.; Liu, Q.; Zhang, Q. Lithium-Anode Protection in Lithium−Sulfur Batteries. *Trends Chem.* **2019**, *1*, 693−704.
(11) Senguttuvan, P.; Han, S.-D.; Kim, S.; Lipson, A. L.; Tepavcevic, S.; Fister, T. T.; Bloom, I. D.; Burrell, A. K.; Johnson, C. S. A High Power Rechargeable Nonaqueous Multivalent Zn/V_2O_5 Battery. *Adv. Energy Mater.* **2016**, *6*, No. 1600826.
(12) Liu, B.; Thoi, V. S. Tailored porous framework materials for advancing lithium-sulfur batteries. *Chem. Commun.* **2022**, *58*, 4005−4015.
(13) Furukawa, H.; Cordova, K. E.; O'Keeffe, M.; Yaghi, O. M. The Chemistry and Applications of Metal−Organic Frameworks. *Science* **2013**, *341*, No. 1230444.
(14) Umeyama, D.; Horike, S.; Inukai, M.; Itakura, T.; Kitagawa, S. Reversible Solid-to-Liquid Phase Transition of Coordination Polymer Crystals. *J. Am. Chem. Soc.* **2015**, *137*, 864−870.
(15) Bennett, T. D.; Tan, J.-C.; Yue, Y.; Baxter, E.; Ducati, C.; Terrill, N. J.; Yeung, H. H. M.; Zhou, Z.; Chen, W.; Henke, S.; Cheetham, A. K.; Greaves, G. N. Hybrid glasses from strong and fragile metal-organic framework liquids. *Nat. Commun.* **2015**, *6*, No. 8079.
(16) Wada, K.; Sakaushi, K.; Sasaki, S.; Nishihara, H. Multielectron-Transfer-based Rechargeable Energy Storage of Two-Dimensional Coordination Frameworks with Non-Innocent Ligands. *Angew. Chem., Int. Ed.* **2018**, *57*, 8886−8890.
(17) Liang, Z.; Qu, C.; Guo, W.; Zou, R.; Xu, Q. Pristine Metal−Organic Frameworks and their Composites for Energy Storage and Conversion. *Adv. Mater.* **2018**, *30*, No. 1702891.
(18) Zhou, C.; Longley, L.; Krajnc, A.; Smales, G. J.; Qiao, A.; Erucar, I.; Doherty, C. M.; Thornton, A. W.; Hill, A. J.; Ashling, C. W.; Qazvini, O. T.; Lee, S. J.; Chater, P. A.; Terrill, N. J.; Smith, A. J.; Yue, Y.; Mali, G.; Keen, D. A.; Telfer, S. G.; Bennett, T. D. Metal-organic framework glasses with permanent accessible porosity. *Nat. Commun.* **2018**, *9*, No. 5042.
(19) Ding, J.; Du, T.; Thomsen, E. H.; Andresen, D.; Fischer, M. R.; Møller, A. K.; Petersen, A. R.; Pedersen, A. K.; Jensen, L. R.; Wang, S.; Smedskjaer, M. M. Metal−Organic Framework Glass as a Functional Filler Enables Enhanced Performance of Solid-State Polymer Electrolytes for Lithium Metal Batteries. *Adv. Sci.* **2024**, *11*, No. 2306698.
(20) Ma, N.; Horike, S. Metal−Organic Network-Forming Glasses. *Chem. Rev.* **2022**, *122*, 4163−4203.
(21) He, B.; Zhang, Q.; Pan, Z.; Li, L.; Li, C.; Ling, Y.; Wang, Z.; Chen, M.; Wang, Z.; Yao, Y.; Li, Q.; Sun, L.; Wang, J.; Wei, L. Freestanding Metal−Organic Frameworks and Their Derivatives: An Emerging Platform for Electrochemical Energy Storage and Conversion. *Chem. Rev.* **2022**, *122*, 10087−10125.
(22) Liu, M.; Liu, T.; Xu, J.; Shao, L.; Shi, X.; Sun, Z. Metal-organic frameworks based solid-state electrolytes for lithium metal batteries: Modifications and future prospects. *Next Energy* **2025**, *6*, No. 100191.
(23) Wu, Q.; Zheng, Y.; Guan, X.; Xu, J.; Cao, F.; Li, C. Dynamical SEI Reinforced by Open-Architecture MOF Film with Stereoscopic Lithiophilic Sites for High-Performance Lithium−Metal Batteries. *Adv. Funct. Mater.* **2021**, *31*, No. 2101034.
(24) Xu, Y.; Gao, L.; Shen, L.; Liu, Q.; Zhu, Y.; Liu, Q.; Li, L.; Kong, X.; Lu, Y.; Wu, H. B. Ion-Transport-Rectifying Layer Enables Li-Metal Batteries with High Energy Density. *Matter* **2020**, *3*, 1685−1700.
(25) Bai, S.; Sun, Y.; Yi, J.; He, Y.; Qiao, Y.; Zhou, H. High-Power Li-Metal Anode Enabled by Metal−Organic Framework Modified Electrolyte. *Joule* **2018**, *2*, 2117−2132.
(26) Moghadam, P. Z.; Li, A.; Wiggin, S. B.; Tao, A.; Maloney, A. G. P.; Wood, P. A.; Ward, S. C.; Fairen-Jimenez, D. Development of a Cambridge Structural Database Subset: A Collection of Metal−Organic Frameworks for Past and Future. *Chem. Mater.* **2017**, *29*, 2618−2625.
(27) Park, K. S.; Ni, Z.; Côté, A. P.; Choi, J. Y.; Huang, R.; Uribe-Romo, F. J.; Chae, H. K.; O'Keeffe, M.; Yaghi, O. M. Exceptional chemical and thermal stability of zeolitic imidazolate frameworks. *Proc. Natl. Acad. Sci. U.S.A.* **2006**, *103*, 10186−10191.
(28) Huang, X.-C.; Lin, Y.-Y.; Zhang, J.-P.; Chen, X.-M. Ligand-Directed Strategy for Zeolite-Type Metal−Organic Frameworks: Zinc(II) Imidazolates with Unusual Zeolitic Topologies. *Angew. Chem., Int. Ed.* **2006**, *45*, 1557−1559.
(29) Tian, Y.-Q.; Zhao, Y.-M.; Chen, Z.-X.; Zhang, G.-N.; Weng, L.-H.; Zhao, D.-Y. Design and Generation of Extended Zeolitic Metal−Organic Frameworks (ZMOFs): Synthesis and Crystal Structures of Zinc(II) Imidazolate Polymers with Zeolitic Topologies. *Chem. - Eur. J.* **2007**, *13*, 4146−4154.
(30) Bennett, T. D.; Yue, Y.; Li, P.; Qiao, A.; Tao, H.; Greaves, N. G.; Richards, T.; Lampronti, G. I.; Redfern, S. A. T.; Blanc, F.; Farha, O. K.; Hupp, J. T.; Cheetham, A. K.; Keen, D. A. Melt-Quenched Glasses of Metal−Organic Frameworks. *J. Am. Chem. Soc.* **2016**, *138*, 3484−3492.
(31) Gómez, M. L. R.; Lampronti, G. I.; Yang, Y.; Mauro, J. C.; Bennett, T. D. Relating structural disorder and melting in complex mixed ligand zeolitic imidazolate framework glasses. *Dalton Trans.* **2020**, *49*, 850−857.
(32) Hou, J.; Gómez, M. L. R.; Krajnc, A.; McCaul, A.; Li, S.; Bumstead, A. M.; Sapnik, A. F.; Deng, Z.; Lin, R.; Chater, P. A.; Keeble, D. S.; Keen, D. A.; Appadoo, D.; Chan, B.; Chen, V.; Mali, G.; Bennett, T. D. Halogenated Metal−Organic Framework Glasses and Liquids. *J. Am. Chem. Soc.* **2020**, *142*, 3880−3890.
(33) Zhou, C.; Stepniewska, M.; Sørensen, J. M.; Scarpa, L.; Magnacca, G.; Boffa, V.; Bennett, T. D.; Yue, Y. Polymorph formation for a zeolitic imidazolate framework composition - $Zn(Im)_2$. *Microporous Mesoporous Mater.* **2018**, *265*, 57−62.
(34) León-Alcaide, L.; Christensen, R. S.; Keen, D. A.; Jordá, J. L.; Brotons-Alcázar, I.; Forment-Aliaga, A.; Mínguez Espallargas, G. Meltable, Glass-Forming, Iron Zeolitic Imidazolate Frameworks. *J. Am. Chem. Soc.* **2023**, *145*, 11258−11264.
(35) Qiao, A.; Bennett, T. D.; Tao, H.; Krajnc, A.; Mali, G.; Doherty, C. M.; Thornton, A. W.; Mauro, J. C.; Greaves, G. N.; Yue, Y. A metal-

https://doi.org/10.1021/acsami.6c03442
ACS Appl. Mater. Interfaces XXXX, XXX, XXX−XXX

organic framework with ultrahigh glass-forming ability. *Sci. Adv.* **2018**, *4*, No. eaao6827.
(36) Gao, C.; Jiang, Z.; Qi, S.; Wang, P.; Jensen, L. R.; Johansen, M.; Christensen, C. K.; Zhang, Y.; Ravnsbæk, D. B.; Yue, Y. Metal−Organic Framework Glass Anode with an Exceptional Cycling-Induced Capacity Enhancement for Lithium-Ion Batteries. *Adv. Mater.* **2022**, *34*, No. 2110048.
(37) Ding, J.; Du, T.; Jensen, L. R.; Sørensen, S. S.; Wang, D.; Wang, S.; Zhang, L.; Yue, Y.; Smedskjaer, M. M. High-Performance Dendrite-Free Lithium Metal Anode Based on Metal−Organic Framework Glass. *Adv. Mater.* **2024**, *36*, No. 2400652.
(38) Frentzel-Beyme, L.; Kloß, M.; Kolodzeiski, P.; Pallach, R.; Henke, S. Meltable Mixed-Linker Zeolitic Imidazolate Frameworks and Their Microporous Glasses: From Melting Point Engineering to Selective Hydrocarbon Sorption. *J. Am. Chem. Soc.* **2019**, *141*, 12362−12371.
(39) Madsen, R. S. K.; Stepniewska, M.; Yang, Y.; Qiao, A.; Winters, W. M. W.; Zhou, C.; König, J.; Mauro, J. C.; Yue, Y. Mixed metal node effect in zeolitic imidazolate frameworks. *RSC Adv.* **2022**, *12*, 10815−10824.
(40) Kühne, T. D.; Iannuzzi, M.; Del Ben, M.; Rybkin, V. V.; Seewald, P.; Stein, F.; Laino, T.; Khaliullin, R. Z.; Schütt, O.; Schiffmann, F.; Golze, D.; Wilhelm, J.; Chulkov, S.; Bani-Hashemian, M. H.; Weber, V.; Borštnik, U.; Taillefumier, M.; Jakobovits, A. S.; Lazzaro, A.; Pabst, H.; Müller, T.; Schade, R.; Guidon, M.; Andermatt, S.; Holmberg, N.; Schenter, G. K.; Hehn, A.; Bussy, A.; Belleflamme, F.; Tabacchi, G.; Glöß, A.; Lass, M.; Bethune, I.; Mundy, C. J.; Plessl, C.; Watkins, M.; VandeVondele, J.; Krack, M.; Hutter, J. CP2K: An electronic structure and molecular dynamics software package - Quickstep: Efficient and accurate electronic structure calculations. *J. Chem. Phys.* **2020**, *152*, No. 194103.
(41) VandeVondele, J.; Krack, M.; Mohamed, F.; Parrinello, M.; Chassaing, T.; Hutter, J. Quickstep: Fast and accurate density functional calculations using a mixed Gaussian and plane waves approach. *Comput. Phys. Commun.* **2005**, *167*, 103−128.
(42) Perdew, J. P.; Burke, K.; Ernzerhof, M. Generalized Gradient Approximation Made Simple. *Phys. Rev. Lett.* **1996**, *77*, No. 3865.
(43) Grimme, S.; Antony, J.; Ehrlich, S.; Krieg, H. A consistent and accurate ab initio parametrization of density functional dispersion correction (DFT-D) for the 94 elements H-Pu. *J. Chem. Phys.* **2010**, *132*, No. 154104.
(44) Goedecker, S.; Teter, M.; Hutter, J. Separable dual-space Gaussian pseudopotentials. *Phys. Rev. B* **1996**, *54*, No. 1703.
(45) Hartwigsen, C.; Goedecker, S.; Hutter, J. Relativistic separable dual-space Gaussian pseudopotentials from H to Rn. *Phys. Rev. B* **1998**, *58*, No. 3641.
(46) Parrinello, M.; Rahman, A. Polymorphic transitions in single crystals: A new molecular dynamics method. *J. Appl. Phys.* **1981**, *52*, 7182−7190.
(47) Nosé, S. A molecular dynamics method for simulations in the canonical ensemble. *Mol. Phys.* **1984**, *52*, 255−268.
(48) Wang, H.; Zhang, L.; Han, J.; E, W. DeePMD-kit: A deep learning package for many-body potential energy representation and molecular dynamics. *Comput. Phys. Commun.* **2018**, *228*, 178−184.
(49) Zeng, J.; Zhang, D.; Lu, D.; Mo, P.; Li, Z.; Chen, Y.; Rynik, M.; Huang, L.; Li, Z.; Shi, S.; Wang, Y.; Ye, H.; Tuo, P.; Yang, J.; Ding, Y.; Li, Y.; Tisi, D.; Zeng, Q.; Bao, H.; Xia, Y.; Huang, J.; Muraoka, K.; Wang, Y.; Chang, J.; Yuan, F.; Bore, S. L.; Cai, C.; Lin, Y.; Wang, B.; Xu, J.; Zhu, J.-X.; Luo, C.; Zhang, Y.; Goodall, R. E. A.; Liang, W.; Singh, A. K.; Yao, S.; Zhang, J.; Wentzcovitch, R.; Han, J.; Liu, J.; Jia, W.; York, D. M.; E, W.; Car, R.; Zhang, L.; Wang, H. DeePMD-kit v2: A software package for deep potential models. *J. Chem. Phys.* **2023**, *159*, No. 054801.
(50) Du, T.; Li, S.; Ganisetti, S.; Bauchy, M.; Yue, Y.; Smedskjaer, M. M. Deciphering the controlling factors for phase transitions in zeolitic imidazolate frameworks. *Natl. Sci. Rev.* **2024**, *11*, No. nwae023.
(51) Liu, S.; Dupuis, R.; Fan, D.; Benzaria, S.; Bonneau, M.; Bhatt, P.; Eddaoudi, M.; Maurin, G. Machine learning potential for modelling H_2 adsorption/diffusion in MOFs with open metal sites. *Chem. Sci.* **2024**, *15*, 5294−5302.
(52) Zhang, Y.; Wang, H.; Chen, W.; Zeng, J.; Zhang, L.; Wang, H.; E, W. DP-GEN: A concurrent learning platform for the generation of reliable deep learning based potential energy models. *Comput. Phys. Commun.* **2020**, *253*, No. 107206.
(53) Zeng, J.; Cao, L.; Xu, M.; Zhu, T.; Zhang, J. Z. H. Complex reaction processes in combustion unraveled by neural network-based molecular dynamics simulation. *Nat. Commun.* **2020**, *11*, No. 5713.
(54) Zhou, Y.; Zheng, H.; Li, W.; Ma, T.; Miao, C. A deep learning potential applied in tobermorite phases and extended to calcium silicate hydrates. *Cem. Concr. Res.* **2022**, *152*, No. 106685.
(55) Zhang, L.; Han, J.; Wang, H.; Saidi, W.; Car, R.et al. In *End-to-End Symmetry Preserving Inter-Atomic Potential Energy Model for Finite and Extended Systems*, Advances in Neural Information Processing Systems; NeurIPS, 2018; p 1.
(56) Thompson, A. P.; Aktulga, H. M.; Berger, R.; Bolintineanu, D. S.; Brown, W. M.; Crozier, P. S.; in 't Veld, P. J.; Kohlmeyer, A.; Moore, S. G.; Nguyen, T. D.; Shan, R.; Stevens, M. J.; Tranchida, J.; Trott, C.; Plimpton, S. J. LAMMPS - a flexible simulation tool for particle-based materials modeling at the atomic, meso, and continuum scales. *Comput. Phys. Commun.* **2022**, *271*, 108171.
(57) Mondal, A.; Kussainova, D.; Yue, S.; Panagiotopoulos, A. Z. Modeling chemical reactions in alkali carbonate−hydroxide electrolytes with deep learning potentials. *J. Chem. Theory Comput.* **2023**, *19*, 4584−4595.
(58) Meher, D.; Avula, N. V. S.; Balasubramanian, S. Slowly quenched, high pressure glassy B_2O_3 at DFT accuracy. *J. Chem. Phys.* **2025**, *162*, No. 044503.
(59) Wang, X.-X.; Guan, D.-H.; Miao, C.-L.; Li, J.-X.; Li, J.-Y.; Yuan, X.-Y.; Ma, X.-Y.; Xu, J.-J. Boundary-Free Metal−Organic Framework Glasses Enable Highly Stable All-Solid-State Lithium−Oxygen Battery. *Adv. Energy Mater.* **2024**, *14*, No. 2303829.
(60) Landgraf, V.; Tu, M.; Zhao, W.; Lavrinenko, A. K.; Cheng, Z.; Canals, J.; de Leeuw, J.; Ganapathy, S.; Vasileiadis, A.; Wagemaker, M.; Famprikis, T. Disorder-Mediated Ionic Conductivity in Irreducible Solid Electrolytes. *J. Am. Chem. Soc.* **2025**, *147*, 18840−18852.
(61) Vasileiadis, A.; Wagemaker, M. Thermodynamics and Kinetics of Na-Ion Insertion into Hollandite-TiO_2 and O_3-Layered $NaTiO_2$: An Unexpected Link between Two Promising Anode Materials for Na-Ion Batteries. *Chem. Mater.* **2017**, *29*, 1076−1088.
(62) de Klerk, N. J.; van der Maas, E.; Wagemaker, M. Analysis of Diffusion in Solid-State Electrolytes through MD Simulations, Improvement of the Li-Ion Conductivity in β-Li_3PS_4 as an Example. *ACS Appl. Energy Mater.* **2018**, *1*, 3230−3242.
(63) Shimakawa, K.; Aniya, M. Dynamics of atomic diffusion in condensed matter: origin of the Meyer−Neldel compensation law. *Monatsh. Chem.* **2013**, *144*, 67−71.
(64) He, X.; Zhu, Y.; Epstein, A.; Mo, Y. Statistical variances of diffusional properties from ab initio molecular dynamics simulations. *npj Comput. Mater.* **2018**, *4*, No. 18.
(65) Koettgen, J.; Zacherle, T.; Grieshammer, S.; Martin, M. Ab initio calculation of the attempt frequency of oxygen diffusion in pure and samarium doped ceria. *Phys. Chem. Chem. Phys.* **2017**, *19*, 9957−9973.
(66) Chen, C.; Lu, Z.; Ciucci, F. Data mining of molecular dynamics data reveals Li diffusion characteristics in garnet $Li_7La_3Zr_2O_{12}$. *Sci. Rep.* **2017**, *7*, No. 40769.
(67) Zhang, Z.; Zou, Z.; Kaup, K.; Xiao, R.; Shi, S.; Avdeev, M.; Hu, Y.-S.; Wang, D.; He, B.; Li, H.; Huang, X.; Nazar, L. F.; Chen, L. Correlated Migration Invokes Higher Na^+-Ion Conductivity in NaSICON-Type Solid Electrolytes. *Adv. Energy Mater.* **2019**, *9*, No. 1902373.
(68) Lavery, R.; Maddocks, J. H.; Pasi, M.; Zakrzewska, K. Analyzing ion distributions around DNA. *Nucleic Acids Res.* **2014**, *42*, 8138−8149.
(69) Sangoro, J. R.; Kremer, F. C. Charge Transport and Glassy Dynamics in Ionic Liquids. *Acc. Chem. Res.* **2012**, *45*, 525−532.
(70) Wiers, B. M.; Foo, M.-L.; Balsara, N. P.; Long, J. R. A Solid Lithium Electrolyte via Addition of Lithium Isopropoxide to a Metal−Organic Framework with Open Metal Sites. *J. Am. Chem. Soc.* **2011**, *133*, 14522−14525.

https://doi.org/10.1021/acsami.6c03442
ACS Appl. Mater. Interfaces XXXX, XXX, XXX−XXX